Cation exchange mediated elimination of the Fe-antisites in the hydrothermal synthesis of $LiFePO_4$

Reference:

Paolella Andrea, Bertoni Giovanni, Hovington Pierre, Turner Stuart, van Tendeloo Gustaaf, et al..- Cation exchange mediated elimination of the Fe-antisites in the hydrothermal synthesis of $LiFePO_4$

Nano energy - ISSN 2211-2855 - 16(2015), p. 256-267

DOI: http://dx.doi.org/doi:10.1016/j.nanoen.2015.06.005

Cation exchange mediated elimination of the Fe-antisites in the hydrothermal synthesis of $LiFePO_4$

*Andrea Paolella, Giovanni Bertoni, Pierre Hovington, Zimin Feng, Roxana Flacau, Mirko Prato, Massimo Colombo, Sergio Marras, Liberato Manna, Stuart Turner, Gustaaf Van Tendeloo, Abdelbast Guerfi, George P. Demopoulos and Karim Zaghib**

Dr. Andrea Paolella, Dr. Pierre Hovington, Dr. Zimin Feng, Dr.Abdelbast Guerfi and Dr. Karim Zaghib
IREQ - Institute Recherche d`HydroQuebec -1800 Boulevard Lionel Boulet, Varennes, QC J3X 1S1
E-mail: zaghib.karim@ireq.ca

Dr. Giovanni Bertoni
IMEM-CNR, Parco Area delle Scienze 37/A, 43124 Parma, Italy

Dr.Roxana Flacau
NRC National Research Council of Canada, Chalk River Laboratories, Chalk River, Ontario K0J 1J0

Dr. Giovanni Bertoni, Dr. Mirko Prato, Dr. Massimo Colombo, Sergio Marras, Prof. Liberato Manna
Istituto Italiano di Tecnologia, via Morego 30, 16130 Genova, Italy

Dr. Stuart Turner, Dr. Gustaaf Van Tendeloo
EMAT, University of Antwerp, Groenenborgerlaan 171, BE 2020 Antwerp, Belgium

Prof. George P. Demopoulos
McGill University, Mining and Materials Engineering Department, Wong Building, 3610 University Street, Montreal QC H3A OC5

Keywords: antisite, LiFePO4, hydrothermal, mechanism, amorphous

Abstract

In this work we elucidate the elimination of mechanism Fe-antisite defects in lithium iron phosphate ($LiFePO_4$) during the hydrothermal synthesis. Compelling evidence of this effect is provided by combining Neutron Powder Diffraction (NPD), High Resolution (Scanning) Transmission Electron Microscopy (HR-(S)TEM), Electron Energy Loss Spectroscopy

(EELS), X-Ray Photoelectron Spectroscopy (XPS) and calculations. We found: i) the first intermediate vivianite inevitably creates Fe-antisite defects in $LiFePO_4$; ii) the removal of these antisite defects by cation exchange is assisted by a nanometer-thick amorphous layer, rich in Li, that enwraps the $LiFePO_4$ crystals.

1. Introduction

After 1997[1] $LiFePO_4$ has attracted much interest as cathode material for Li-ion batteries because of its superior safety, its high theoretical capacity (~ 170 mAh g^{-1}), its high stability and its suitable operating voltage (~3.4 V). Olivine has a structure with *Pnma* space group where lithium is confined in channels (M1 site) formed by the interconnection of FeO_6 octahedra (M2 site) and PO_4 tetrahedra. Since the initial solid-state synthesis method reported in 1997 by John B. Goodenough,[1] $LiFePO_4$ has been synthesized using many different methods: as hydrothermal,[2] solvothermal,[3] sol-gel,[4] co-precipitation[5] and colloidal[6] methods. $LiFePO_4$ has however some critical limitations related to its poor ionic[7] and electronic conductivity[8] that are partially overcome by carbon coating,[9] by doping with several cations (V^{5+}, Mg^{2+}, Ti^{4+}, Zr^{4+}, Nb^{5+}),[10,11] by particles nanosizing[12] or by the crystalline habit optimization if exposing the [010] facets for short diffusion length of Li^+ ions through 1D channels along b-axis.[13,14] Despite all the recent developments in the synthesis of $LiFePO_4$, the hydrothermal route remains the lowest cost method to synthesize $LiFePO_4$.[15-17] One of the main unsolved issues of the hydrothermally synthesized $LiFePO_4$ relates to the formation of Fe-antisite defects that preferentially form at low temperature.[15] Hydrothermal synthesis usually requires long synthesis time or a post synthetic annealing treatment to remove these obstacles for Li-ion diffusion pathway.[2] After Graetz`s in-situ X-ray diffraction studies of $LiFePO_4$ antisite defects,[18,19] Iversen and co-workers demonstrated using neutron scattering[20] that the antisite defects are mainly constituted of Fe-ions in M1 space without

any presence of Li-ions in M2 spaces. Other studies sought to clarify and control the role of antisites: making use of vanadium[21,22] or niobium dopants,[23] thermal annealing[24] or first principle calculations.[25,26] Fe^{2+} occupying the M1 sites in anisotropic manner[23,27] is therefore an obstacle to the removal of lithium causing so a degradation of the electrochemical performance. In this work, we study the formation and the removal of Fe-antisite defects of $LiFePO_4$ during its hydrothermal synthesis, present comprehensive observational investigations via a combination of experimental techniques, explain the evolution of the intermediate products with interfacial cation exchange mechanism and finally attempt to support our idea with theoretical calculations. The mechanism here proposed is based on an interfacial cations exchange reaction, which has not been reported previously. The mechanism involves as first step the formation of energetically favoured antisite-$LiFePO_4$ defects (occupancy of M1 sites by Fe (II)), which are subsequently eliminated upon lithium insertion (Fe out Li in exchange) to yield defect free $LiFePO_4$ (~ 100% Li in M1 sites). Most importantly the cation-exchange process involves Li ions initially present in an amorphous layer which covers the crystal, i.e. it happens at the crystal/amorphous interfacial zone. By theoretical calculations, the presence of the amorphous layer is indispensible for promoting the cation exchange reaction. Obviously understanding the mechanism of the formation and the removal of Fe-antisite defects in $LiFePO_4$ is a crucial step for the development of low cost high performing $LiFePO_4$ cathode material by water-based synthesis[28] instead of those with more expensive organic solvents like ethylene glycol[29] or ethanol.[30] The crystal structures of all the hydrothermally synthesized $LiFePO_4$ samples was determined using X – ray diffraction (XRD) while the morphology of the crystals was followed by scanning electron microscope (SEM), high resolution electron transmission microscopy (HR-TEM) and scanning transmission electron microscopy (STEM). The surface area evolution was followed by Brunauer-Emmett-Teller (BET) analysis. The antisite defects were monitored via neutron powder diffraction (NPD) and high angle annular dark field (HAADF). The lithium and iron

contents in the crystals were characterized via X-ray photoelectron spectroscopy (XPS) and electron energy loss spectroscopy (EELS) techniques. The energetic profile of the reaction was computed by density functional theory (DFT) combined with the continuum solvation model (CSM).

2. Results

Samples were collected at different intermediate steps of the hydrothermal $LiFePO_4$ synthesis, i. e. 10 min, 15 min, 30 min and 5h, as described in the Experimental Methods section. **Figure 1a** shows the SEM image of the 10 minutes intermediate revealing the formation of plate like crystals surrounded by many fibers. According to the XRD pattern (**Figure 1e**), the first intermediate shows the presence of crystalline vivianite $Fe_3(PO4)_2 \cdot 8H_2O$ (PDF card number 9010966, space group *C 1 2/m 1 (12)*) and triphylite $LiFePO_4$ (PDF card number 01 – 078 – 3313, space group *Pnma (62)*). The result is in agreement with literature,[19,31,32] indicating that an Fe-rich phase, i.e.vivianite $Fe_3(PO4)_2 \cdot 8H_2O$, is the first one forming during the hydrothermal synthesis of $LiFePO_4$. At 15 minutes, the XRD pattern shows only triphylite $LiFePO_4$ phase while the SEM image (**Figure 1b**) shows the presence of submicron crystals plate shaped and hollow particles. At 30 minutes the $LiFePO_4$ crystals seemed (SEM in **Figure 1c** and XRD in **Figure 1e**) to have grown and densified considerably, although some small hollow-like crystallites are still present. At 5 hours the $LiFePO_4$ crystals have fully grown to thick plate-shaped particles (**Figure 1d**).

Figure 2 shows HRTEM and STEM images of the evolving $LiFePO_4$ crystals. HRTEM image in **Figure 2a** shows the surface of a crystal at 15 minutes. A nano-metric amorphous layer is present at this stage, with an average thickness of 3.2 ± 0.9 nm (see the **Table 1**). STEM acquired on several crystals reveals that the $LiFePO_4$ crystals are porous, presenting large and small holes (**Figure 2d**). The corresponding BET surface area is $7.3 m^2/g$ (see **Table**

1). At 30 minutes, the STEM image (**Figure 2e**) shows less porous $LiFePO_4$ particles, compared to the $LiFePO_4$ 15 minutes intermediate (as confirmed by BET data analysis $6.3m^2/g$ vs $7.3m^2/g$). The amorphous layer around the $LiFePO_4$ particles has decreased too, with an average thickness of 1.6 ± 0.5 nm (HRTEM image in **Figure 2b**). Finally the sample collected after 5 hours (STEM in **Figure 2e**) shows crystals with low or no sign of porosity and the BET surface data at this stage is 5.4 m^2/g. At the same time the average amorphous layer thickness (HRTEM in **Figure 2c**) is statistically decreased to 1.1 ± 0.2 nm. As first summary: we observed a decrease of the amorphous shell thickness with crystal growth progress (15 minutes to 5 hours): from an average value of 3.2 ± 0.9 nm to 1.1 ± 0.2 nm with a decrease of the surface area from 7.3 m^2/g to 5.4 m^2/g. Considering the presence of the amorphous layer around the crystals we advance the idea that the transformation of the initially nucleated vivianite $Fe_3(PO4)_2 \cdot 8H_2O$ to $LiFePO_4$ occurs though its amorphization by gathering of Li-ions.

The **Table 1** gives the lithium and iron content evolution during the synthesis as measured from EELS. At 15 minutes EELS quantification gives a ratio between Fe/Li close to 1, while the ratio Fe/P is 1.3, in agreement with a mechanism considering vivianite $Fe_3(PO4)_2 \cdot 8H_2O$ as the first precursor seed of $LiFePO_4$ (in $Fe_3(PO4)_2 \cdot 8H_2O$ the ratio Fe/P is 1.5) previous the amorphization following the addition of lithium ions. At 30 minutes we observe the presence of a strong excess of lithium compared to iron (Fe/Li = 0.70) while at this stage the ratio Fe/P is close to 1 and the Fe/O is close to 0.25. These ratios point out to for $LiFePO_4$ in agreement with XRD findings. After 5 hours the amount of lithium is decreased and the Fe/Li ratio is close to 1. The oxidation state of Fe in all the sample (both core and shell) is always found around (II) as measured approximately[6] from the Fe $L_{2,3}$ white lines ratio (see **Figure 3**). In order to gain some more insights on the nature of the amorphous shell around the particles, all the samples were also analysed using X-ray photoelectron spectroscopy (XPS).

X-ray photoelectron spectroscopy is a well-know technique for qualitative and quantitative analysis of the surface chemistry (i.e. 5-10 nm in depth) of the samples under investigation. XPS peaks' shapes and positions can provide useful information on the local environment of atoms and their oxidation states, while peaks areas can be used for measuring the stoichiometry of the analysed samples.

In the present report, XPS analysis mainly focused on the study of the evolution of Fe oxidation state as well as of the Li/Fe atomic ratio as a function of the reaction time (15 minutes, 30 minutes and 5 hours). For this purpose, high resolution spectra were collected on Fe 2p, Fe 3s and Fe 3p core levels, together with the main lines for oxygen and phosphorous (O 1s and P 2p, respectively). The spectra for Fe 2p, O 1s and P 2p lines are reported in the supporting information. Here we focus the analysis on Fe 3s and 3p lines. In particular, the peculiar shape of the Fe 3s profile is characteristic of Fe(II). Indeed, as explained by Gonbeau et al.,[33] the observed splitting of the Fe 3s peak into two components results from the exchange interaction of Fe 3s and 3d electrons, leading to an energy difference between two photoemission final states with the 3s spin parallel or antiparallel to the 3d spin. Since the energy separation between the components strictly depends on number of the 3d electrons, it can be used as parameter to assign the Fe oxidation state.

For all the analysed samples, the energy separation is 5.65 (±0.05) eV (as shown in **Figure 4** - left panel), in close agreement with the expected value for Fe(II) (i.e. 5.7 eV). As reference, the expected value for Fe(III) is about 6.5 eV.[33] Obviously, it is not possible to completely exclude the presence of tiny amount of Fe(III); however, based on our XPS data, we can conclude that Fe is present mainly as Fe(II) in all the investigated samples, as confirmed also by the position of the Fe 3p peak at 55 eV and by analysis of Fe 2p lines[34] (see Supporting Information).

Regarding the Li/Fe ratio, it is well known that the main Li line (i.e. Li 1s) is usually buried in the Fe 3p peak, and it can hardly be observed since its relative sensitivity factor (RSF, a

parameter that can be related to the cross section of the X-ray induced photoemission process) is extremely low with respect to that of the Fe 3p line (in the present case 15 times smaller, 0.025 vs. 0.37). Even if it was recently reported by Liu et al.,[35] identification of the Li 1s is therefore complicated, the problem being compounded due to the multiplet structure of the Fe 3p line. Here we propose an alternative method for Li quantification, based on the comparison of the areas of the Fe 3s and Fe 3p lines. As we are referring to the same element, the same Fe quantification (within the experimental error) should be obtained by analysing the two different lines. Moreover, the two lines are also close in binding energy, so we can safely assume that the information is coming from the same analysis depth. Under these hypothesis, we decided to assign to Li the possible overestimation of Fe when analysizing Fe 3p line. Note that the Li content cannot be obtained directly as the difference between the two quantifications, without performing a "calibration" for the Li 1s RSF. The outcome of the method is graphically depicted in **Figure 4** (right panel), where the experimental profiles for Fe 3p peaks are reported (as markers) together with the corresponding scaled profiles (continuous lines). Scaling factor is such that the Fe quantification based on the scaled profile is exactly the same with that obtained by analysing the Fe 3s peaks (i.e. it corresponds to the ratio of the areas of the Fe 3s and Fe 3p experimental profiles, as reported in **Table S1** in supporting information). Please note that the scaled profile is not the result of a deconvolution procedure and it does not represent the exact shape of the Fe 3p component. The difference in area between the experimental and the scaled profiles (shaded areas in the **Figure 4**) has been assigned to the Li content, under our hypothesis. As seen in **Table S1** the sample at 30 minutes is the one with the highest Li content; the 15 minutes and the 5 hours samples show a similar Li content. To obtain the true Li/Fe ratio, the observed differences between Fe 3p and Fe 3s areas have been multiplied by the ratio between the Fe 3p and Li 1s RSFs. In this way, we obtained a Li/Fe ratio of 2.3, 3.1 and 2.3 for the 15 minutes, 30 minutes and 5 hours samples, respectively. The XPS analysis therefore suggests that Li is present in large excess in

the surface for all the samples. Moreover, by comparing the XPS quantification with EELS quantification, we could infer that the Li excess is mainly located at the surface of the particles. We can propose that the amorphous shell is a lithium-rich layer that is progressively consumed with time, i.e. as the $LiFePO_4$ crystals grow. On the basis of our EELS/XPS observations we argue that the antisite defects are gradually removed with the replacement of Fe in M1 by lithium coming from the amorphous shell.

In order to quantify the percentage of Fe-antisites in the structure we have performed neutron powder diffraction measurements. Data analysis was carried out for patterns collected on the 15 min, 30 min and 5h samples and in all cases $LiFePO_4$ was found to be the only phase present. Given that both EELS and XPS analysis suggest that the oxidation state for Fe is (II) for all the intermediate samples, thus excluding the presence of any Fe (III) species that could show the presence of extra Li-vacancies (see supporting information). The Rietveld refinements were performed by under the following constrain: occupancy (Li-M1) = 1-2*occupancy(Fe-M1). **Figure 5a** shows the Fe-M1 occupancy as a function of the synthesis time. The occupancy drops from 8% at an early stage in the synthesis (15 min) to 2% at the final stage (5h). The Rietveld refinement (see **Figure S2** and **Table S3** in the supporting information) of the $LiFePO_4$ 15 minutes intermediate sample shows 8% of Fe occupancy at the M1 site (along the *b* channel - see supp info and **Figure 5a**) in agreement with volume change while no Li ions occupancy are detected in M2 with a fully occupancy by Fe - ions. The following Rietveld refinement for $LiFePO_4$ intermediate collected after 30 minutes (see **Figure S3** and **Table S4** in supporting information) shows that the Fe occupancy in M1 falls to 4% from 8% while for $LiFePO_4$ after 5 hours the Fe occupancy in M1 further decreases to 2% (see **Figure S4** and **Table S5** in supporting information). **Figure 5b** shows the evolution of the unit cell volume as function of the Fe occupancy as observed via Rietveld refinements. The volume of the unit cell is decreasing with the decrease of Fe occupancy of M1 site, as

expected when substituting a heavier atom with a lighter one (**Figure 5b).** The refined structural parameters for all three intermediate samples (**Tables S2-S4**) and the Rietveld plots (**Figure S2-S4**) can be found in the Supporting Information.

We would like to emphasize the fact that the standard error deviations of Li and Fe occupancies as reported from the Rietveld refinements are significantly lower than the actual measurement errors intrinsic to neutron powder diffraction. By calculating the NPD patterns for various Li and Fe site occupancies, using resolution and statistics similar with our experimental ones, we estimate the error associated with Fe occupancy to be 1.5% and that for Li occupancy around 10%. Below these values no significant changes have been observed in the relative intensities of the calculated patterns and they are not unexpected given the scattering lengths of Fe and Li, 9.45 and -1.9 fm, respectively. Hence, 1.5% is the error considered in **Figure 5a** (see supporting information). Also it's important to consider that the total decrease of the Fe-antisite can be lower than the decrease that appears by NPD data: the $LiFePO_4$ 15 minutes intermediate has a surface area higher than $LiFePO_4$ after 5 hours (7.3 m^2/g at 15 minutes vs 5.4 m^2/g at 5 hours, with a decrease of 27% in surface area) that means that the 8% of Fe – occupancies in M1 are distributed in a smaller volume compared to the 2% of Fe – occupancy in M1 observed at 5 hours. To confirm the results from neutron scattering, we performed HAADF-STEM[28,35,36] to directly image the Fe-antisites defects (see **Figure 6**) from [010] oriented crystals, in which M1 (Li) and M2 (Fe) columns can be imaged separately. Indeed, at the condition of imaging (inner cut-off angle of the detector 50 mrad) the Li columns should appear dark, while the Fe columns should appear bright (see the simulation from a defect free LFP in **Figure 6b**). Fe-antisites at M1 are easily spotted as unexpected bright columns. However, only a relative high amount of Fe substitution (around 10%) is sufficient to give a measurable variation in the contrast.[37] **Figure 6a** shows the experimental image of $LiFePO_4$ collected after 15 minutes. Bright columns at M1 sites are

indeed visible almost everywhere, and are in agreement with a simulation with statistical substitution of 8% of Fe in M1 as measured form NPD (see the simulation in **Figure 6c**).

2.1. Mechanism of Fe-antisite defects elimination

The antisite evolution obtained via neutron powder diffraction can be understood in connection to the EELS and XPS analysis. At 15 minutes the ratio Li/Fe is close to 1 according to EELS while the ratio is 2.3 according to XPS. Moreover considering that the amorphous layer thickness is 3.2 nm thick and XPS is penetrating for 5 nm, it becomes evident that the amorphous layer is much richer in lithium than the core of the crystal. At 30 minutes the ratio Li/Fe is close to 1.5, according to EELS so there is an increase in lithium content at this stage. On the other end XPS gave a ratio Li/Fe equal to 3.1 while this time the thickness of the amorphous layer thickness is 1.6 nm, approximately half of that of the 15 minutes intermediate. After 15 minutes the lithium ions are seen to have penetrated into the crystal while excess of lithium is accumulated at the surface. After 5 hours, the ratio Li/Fe is 1 by EELS while the ratio decreased at 2.3 by XPS. Furthermore the thickness of the amorphous layer is reduced to 1.1 nm, meaning that lithium is entered inside the crystal. This is in agreement with the data observed by neutron pattern diffraction that indicated Fe-antisite after 5 hours of the synthesis to have been reduced to <2%. Summarizing all the data reported above: we observe a gradual decrease of the external amorphous layer thickness (from 3.2 nm at 15 minutes to 1.1 nm at 5 hours), the variation of the lithium content at the amorphous layer (by XPS and EELS analysis), and the removal of Fe –antisites defects by NPD (from 8% at 15 minutes to 2% at 5 hours). On the basis of these observations we hypothesize that the removal of the Fe-antisites occurs at the interface between pure $LiFePO_4$ (no antisite present) and the external amorphous layer. The Fe-antisite defects are thought to occupy a sub surface zone from which are gradually corrected by a cations - exchange reaction: Fe ions in M1 site that

are replaced by Li-ions present in excess in the amorphous layer in strict contact with the crystals creating a favorable diffusion gradient. **Figure 7** provides a graphical illustration of the proposed mechanism. Also considering the decrease in thickness of the amorphous layer, we suppose that Fe ions in M1 sites can be involved in a subsequent new crystallization of $LiFePO_4$ after the interfacial cation-exchange reaction.

2.2. Calculations

Our experimental observations can be further supported by the theoretical calculations. **Figure 8** shows the calculated energy profile of vivianite ($Fe_3(PO4)_2 \cdot 8H_2O$), antisite iron phosphate ($Fe_3(PO4)_2$, 100% Fe occupancy in M1 sites, named as AFP in **Figure 8**), $LiFePO_4$ with 12.5% of Fe occupancy in M1 sites (named as ALFP in **Figure 8**) and stoichiometric $LiFePO_4$ (named as LFP in **Figure 8**). According to our calculation (see Methods for more details), the dehydration of vivianite to form orthorhombic full Fe-antisite iron phosphate (AFP) is energetically favourable. This process reduces the total energy by -4eV per four formula units in the aqueous solution. This produces the undesirable antisite-defects issue. Nevertheless, to produce stoichiometric $LiFePO_4$ (LFP) in the aqueous solution by replacing those Fe ions in the M1 sites with Li ions requires a huge energy input. As is shown in **Figure 8**, it takes +19eV per four formula units to reach a purity of 78.5% in $LiFePO_4$ (ALFP); and to produce pure LFP it takes additional +3eV.

The origin of this large energy raise lies in the fact that it takes +8.8eV of energy to repel a Fe^{2+} ion into the aqueous solution while it takes another +1.9eV of energy to grasp a Li^+ ion from the aqueous solution, i.e., Fe^{2+} ions tend to stay in the crystal while Li^+ ions tend to stay in the water (see the Methods section for computational details). To replace the Fe ions in full orthorhombic Fe-antisite $Fe_3(PO4)_2$ (AFP) with Li ions involves both pushing an Fe^{2+} ion out to the water and absorbing a Li^+ ion in from the water, which unfortunately reverses both trends, hence the high energy need is resulted.

Thus this energy profile in **Figure 8** explains the quick and inevitable formation of antisite iron phosphate ($Fe_3(PO4)_2$) as an intermediate product from vivianite but leaves us with the question: why pure $LiFePO_4$ is formed anyway?

To address this, we carried out another calculation on the effect of the amorphous layer and it shows that it is the amorphous layer that facilitated the removal of Fe-antisite defects. The amorphous layer is assumed to have a Li^+/Fe^{2+} ratio of 2:1, in accordance with the experimental observation. The charge is balanced by PO_4^{3-} anions. We found that the cation-exchange between the AFP and the amorphous layer is much easier. In particular, it takes only +2.4eV to repel an Fe^{2+} ion from the AFP into the amorphous structure while there is an energy gain of -1.6eV to absorb a Li^+ ion from the amorphous structure into the AFP. This huge difference comes from the fact that the cation has to overcome the strong electrostatic interaction in order to flee the crystal, while the latter isn't required in the cation exchange between AFP and the covering amorphous layer. Given these results, we conclude that there is an overall energy gain of -1eV per four formula units of $LiFePO_4$ to be formed out from this ion exchange mechanism.

From a kinetics point of view, the cation-exchange is orders of magnitude slower than the simple dehydration, therefore vivianite ($Fe_3(PO4)_2 \cdot 8H_2O$) has to transform into AFP ($Fe_3(PO4)_2$) first and a direct transformation to pure $LiFePO_4$ cannot happen because of the much longer time the ion exchange mechanism requires. Qualitatively, the covering amorphous layer facilitates the cation-exchange with its wrapped crystal. But as the cation-exchange reaction goes on and the amorphous layer gets thinner and wetter, the facilitating effect of the amorphous layer gradually diminishes, or in terms of the energy profile in **Figure 8**, the energy of pure $LiFePO_4$ within the amorphous layer (the bottom-right bar) gradually raises. This slows down the ion exchange, which is exactly what we observed in the experiments.

3. Conclusion

We presented a mechanism of Fe-antisite defects elimination from $LiFePO_4$ via cation-exchange based on experimental results of XRD, STEM, EELS, XPS and NPD, which has not been reported previously. We have demonstrated that the Fe-antsites defects to be removed should be located at the surface as surface defects. By calculation, an amorphous layer strict in contact with the crystal helps eliminating the Fe-antisite defects by facilitating the ion exchange. Actually the long synthetic time requested by the hydrothermal route (5- 7 hours) is mainly dedicated to the elimination of the Fe-antisites via cation-exchange reaction as demonstrated by our experiments. All these studies are important in order to generate future fast and then low cost synthesis of defect free $LiFePO_4$ cathode materials by passing the initial formation of vivianite that is responsible of the formation of Fe-antisite defects.

4. Experimental Methods

Chemicals Iron sulphate heptahydrate $FeSO_4 \cdot 7H_20$ (purity $\geq$ 99.0%), Lithium hydroxide monohydrate $LiOH \cdot H_20$ (purity $\geq$ 98.0%), phosphoric acid H_3PO_4 (85% w/w in water, $\geq$99.9 % trace metals basis), ammonium hydroxide NH_4OH (solution 28.0-30.0% NH_3 basis) and ascorbic acid $C_6H_8O_6$ (purity $\geq$ 99.0%) were purchased by Sigma Aldrich.

Synthesis of hydrothermal samples In 300 ml of ultrapure (18 MΩ cm^{-1}) deionised water 33.6 gr (0.12 mol) of $FeSO_4 \cdot 7H_20$, 15,41 gr (0.36 mol) of $LiOH \cdot H_20$, 13,83 gr (0.12 mol) of H_3PO_4, 0.5 gr of Ascorbic Acid were mixed. The final molar ratio between Li : Fe : PO_4 : $C_6H_8O_6$ was 3 : 1 : 1 : 0.008. The pH was controlled at 7.8 dropping NH_4OH. All the synthesis were performed in a glass liner using a stirring autoclave (OM-JAPAN). In a classical synthesis, starting from room temperature the solution in the autoclave was heated to 180 degrees in around 30 minutes and subsequently heated at 180ºC for 5 hours. At 180ºC the gas

pressure was around 1 MPa (approximately 10 atm) and the rate stirring was fixed at 800 rpm. After cooling, the final dispersion was filtered at 0.45 μm adding fresh deionised water and ethanol to remove the residual of ascorbic acid. The filtering was followed by drying at 90 °C for 3 h under N2 ambient We collected intermediates at different time in the heating ramp: so we collected a sample after 10 minutes of synthesis (with an approximate temperature reached of 90 ºC), 15 minutes (at a temperature reached of 120ºC) and 30 minutes (at the end of the heating ramp so the temperature was 180ºC).

X - Ray Diffraction Powders were characterized using X-ray diffraction (XRD) analysis in the 2θ range 10 - 120° with scan rate of 0.025 θ min $^{-1}$ on a Rigaku (PW3050) diffractometer equipped with a Co anticathode (Co *Kα* radiation λ = 0.178897 nm) at room temperature.

Scanning Electron Microscopy The surface morphology and particle size of the samples were observed using a cold field emission S-4700 scanning electron microscope (SEM) from Hitachi (Japan).

Brunauer- Emmett- Teller (BET) measurements. Specific surface area measurements were carried out by nitrogen physisorption at 77 K in a Quantachrome equipment, model autosorb iQ. The specific surface areas were calculated using the multi-point BET (Brunauer–Emmett–Teller) model, considering 11 equally spaced points in the P/P_0 range of 0.05 to 0.35. Prior to measurements, samples (50 to 200 mg in form of powder) were degassed for 1 hour at 30°C under vacuum to eliminate weakly adsorbed species.

Transmission Electron Microscopy (TEM). High Resolution TEM (HRTEM), electron energy loss spectroscopy (EELS), and scanning TEM (STEM) measurements were acquired with a JEOL JEM-2200FS microscope equipped with a Schottky emitter at 200 kV, a CEOS

aberration corrector in the objective lens, and an in-column energy Ω-filter. For the details of EELS quantification and Fe oxidation state extraction, the reader is referred to our recent paper.[6] High angle annular dark field images (HAADF) were acquired on a FEI Titan 'cubed' microscope equipped with a CEOS probe corrector. The condition of imaging were 300 kV electron beam energy, 21 mrad probe aperture, and 0.08nm probe size. The acceptance angle of the annular detector was set to 50-160 mrad. Simulations of the images were performed using STEM-CELL using linear approximation.[38]

X-ray Photoelectron Spectroscopy (XPS). XPS was performed on a Kratos Axis Ultra DLD spectrometer, using a monochromatic Al Kα source (15 kV, 20 mA). Wide scans were acquired at analyzer pass energy of 160 eV. High resolution narrow scans were performed at constant pass energy of 10 eV and steps of 0.1 eV. The photoelectrons were detected at a take-off angle Φ = 0° with respect to the surface normal. The pressure in the analysis chamber was maintained below 7×10^{-9} torr for data acquisition. The data were converted to VAMAS format and processed using Casa XPS soft-ware, version 2.3.16. The binding energy (BE) scale was internally referenced to the C 1s peak (BE for C-C = 284.8 eV).

Neutron powder diffraction (NPD) The patterns were collected at C2 High Resolution Powder Diffractometer, NRU reactor, Chalk River Laboratories at room temperature conditions, using vanadium sample cans. The instrument is equipped with an 800-wire position-sensitive detector covering a range of 80 degrees. 1.328 Å wavelength neutrons were used to measure the data in 2θ range of 5 to 117 degrees, with a step size of 0.1 degrees. The patterns were then analysed using FullProf Suite.[39]

Calculation To further investigate the reaction pathways, we carried out calculations on the energy changes between these compounds. This calculation contains two parts: the first

principle density functional theory (DFT)[40,41] calculations of the bulk energies of those compounds and the continuum solvation model[42] calculation of the solvation free energies of the cations in aqueous solution. The latter is needed because there are molecule/ion exchanges between the compounds and their aqueous environment. The DFT calculation of crystalline vivianite and full Fe-antisite $LiFePO_4$ (AFP in **Figure 8**) is done through the VASP package[43] using the projector augmented wave scheme.[44,45] To correctly capture the iron atom's d-electron features, we used Perdew-Burke-Ernzerhof functional[46] with Hubbard U correction,[47] where U=3.7eV for Fe^{2+} ions, in accordance with the suggestion by Zhou et. al.[48] There are known deviations of the value of U for different crystal structures,[48] but our test shows that such deviations only causes slight changes in total energies and therefore we used U=3.7eV for all structures. The energy change for the ion exchange between AFP and the amorphous layer is done with the structure shown in **Figure S5.** We put an AFP layer next to an amorphous layer in the supercell (24.6Å×12.3Å×10.5Å) and computed the energy difference between a Fe vacancy is put in the AFP and in the amorphous structure. The energy change for Li is calculated in the same way. The continuum solvation model calculation is done through the GAMESS package,[49] using the 6-31G basis set.[50] The radii for the cavities of Li+ and Fe2+ are chosen to be 1.3 Angstrom and 2.0 Angstrom, well in line with the suggestions from Refs.[51,52] and the cavity of the water molecule is chosen via the COSMO method.[53] We found that alternative choices of cavity sizes within a reasonable range do not change our results in a qualitative way.

Supporting Information

Supporting Information is available from the Wiley Online Library or from the author.

Acknowledgements

The authors want to acknowledge prof. Ashok Vijh, Vincent Gariepy, Catherine Gagnon, Julie Trottier, Daniel Clement, dr. Timochevski Vladimir, dr. Bruno Rousseau, dr. Cyril Faure

of IREQ, prof. Micheal Armand of CICenergigune for helpful discussions and technical supports.

Author contributions

Andrea Paolella and Giovanni Bertoni equally contributed to this work

References

[1] A. K. Padhi, K. S. Nanjundaswamy, J. B. Goodenough, *J. Electrochem. Soc.* **1997**, *144*, 1188.
[2] S. F. Yang, Y. N. Song, P. Y. Zavalij, M. S. Whittingham, *Electrochem. Commun.* **2002**, *4*, 239.
[3] L. Wang, X. M. He, W. T. Sun, J. L. Wang, Y. D. Li, S. S. Fan, *Nano Lett.* **2012**, *12*, 5632.
[4] K.-F. Hsu, S.-Y. Tsay, B.-J. Hwang, *J. Mater. Chem.* **2004**, *14*, 2690.
[5] K. S. Park, K. T. Kang, S. B. Lee, G. Y. Kim, Y. J. Park, H. G. Kim, *Mater. Res. Bull.* **2004**, *39*, 1803.
[6] A. Paolella, G. Bertoni, S. Marras, E. Dilena, M. Colombo, M. Prato, A. Riedinger, M. Povia, A. Ansaldo, K. Zaghib, L. Manna, C. George, *Nano Lett.* **2014**, *14*, 6828.
[7] P. S. Herle, B. Ellis, N. Coombs, L. F. Nazar, *Nat. Mater.* **2004**, *3*, 147.
[8] P. P. Prosini, M. Lisi, D. Zane, M. Pasquali, *Solid State Ionics* **2002**, *148*, 45.
[9] J. J. Wang, X. L. Sun, *Energy Environ. Sci.* **2012**, *5*, 5163.
[10] S. Y. Chung, J. T. Bloking, Y. M. Chiang, *Nat. Mater.* **2002**, *1*, 123.
[11] C.-Y. Chiang, H.-C. Su, P.-J. Wu, H.-J. Liu, C.-W. Hu, N. Sharma, V. K. Peterson, H.-W. Hsieh, Y.-F. Lin, W.-C. Chou, C.-H. Lee, J.-F. Lee, B.-Y. Shew, *J. Phys. Chem. C* **2012**, *116*, 24424.
[12] K. T. Lee, W. H. Kan, L. F. Nazar, *J. Am. Chem. Soc.* **2009**, *131*, 6044.
[13] X. H. Rui, X. X. Zhao, Z. Y. Lu, H. T. Tan, D. H. Sim, H. H. Hng, R. Yazami, T. M. Lim, Q. Y. Yan, *Acs Nano* **2013**, *7*, 5637.
[14] D. Morgan, A. Van der Ven, G. Ceder, *Electrochem. Solid-State Lett.* **2004**, *7*, A30.
[15] J. J. Chen, M. S. Whittingham, *Electrochem. Commun.* **2006**, *8*, 855.
[16] X. Qin, X. H. Wang, H. M. Xiang, J. Xie, J. J. Li, Y. C. Zhou, *J. Phys. Chem. C* **2010**, *114*, 16806.
[17] B. Ellis, W. H. Kan, W. R. M. Makahnouk, L. F. Nazar, *J. Mater. Chem.* **2007**, *17*, 3248.
[18] J. J. Chen, J. Graetz, *ACS Appl. Mater. Interfaces* **2011**, *3*, 1380.
[19] J. J. Chen, J. M. Bai, H. Y. Chen, J. Graetz, *J. Phys. Chem. Lett.* **2011**, *2*, 1874.
[20] K. M. O. Jensen, M. Christensen, H. P. Gunnlaugsson, N. Lock, E. D. Bojesen, T. Proffen, B. B. Iversen, *Chem. Mater.* **2013**, *25*, 2282.
[21] F. Omenya, N. A. Chernova, Q. Wang, R. B. Zhang, M. S. Whittingham, *Chem. Mater.* **2013**, *25*, 2691.
[22] K. Y. Park, I. Park, H. Kim, H. D. Lim, J. Hong, J. Kim, K. Kang, *Chem. Mater.* **2014**, *26*, 5345.
[23] S. Y. Chung, S. Y. Choi, T. Yamamoto, Y. Ikuhara, *Angew. Chem., Int. Ed.* **2009**, *48*, 543.

[24] S. Hamelet, M. Casas-Cabanas, L. Dupont, C. Davoisne, J. M. Tarascon, C. Masquelier, *Chem. Mater.* **2011**, *23*, 32.
[25] M. S. Islam, D. J. Driscoll, C. A. J. Fisher, P. R. Slater, *Chem. Mater.* **2005**, *17*, 5085.
[26] K. Hoang, M. Johannes, *Chem. Mater.* **2011**, *23*, 3003.
[27] S.-Y. Chung, S.-Y. Choi, T.-H. Kim, S. Lee, *ACS Nano* **2015**, *9*, 850.
[28] J. Wang, X. Sun, *Energy Environ. Sci.* **2015**
[29] X. Qin, J. M. Wang, J. Xie, F. Z. Li, L. Wen, X. H. Wang, *Phys. Chem. Chem. Phys.* **2012**, *14*, 2669.
[30] M. Y. Cho, K. B. Kim, J. W. Lee, H. Kim, H. Kim, K. Kang, K. C. Roh, *RSC Adv.* **2013**, *3*, 3421.
[31] Z. J. Li, K. J. Zhu, J. L. Lia, X. H. Wang, *Crystengcomm* **2014**, *16*, 10112.
[32] L. Lin, Y. Q. Wen, J. K. O, Y. Guo, D. Xiao, *RSC Adv.* **2013**, *3*, 14652.
[33] R. Dedryvere, M. Maccario, L. Croguennec, F. Le Cras, C. Delmas, D. Gonbeau, *Chem. Mater.* **2008**, *20*, 7164.
[34] A. P. Grosvenor, B. A. Kobe, M. C. Biesinger, N. S. McIntyre, *Surf. Interface Anal.* **2004**, *36*, 1564.
[35] W. Xiong, Q. Hub, S. Liu, *Anal. Methods* **2014**, *6*, 5708.
[36] A. Paolella, G. Bertoni, E. Dilena, S. Marras, A. Ansaldo, L. Manna, C. George, *Nano Lett.* **2014**, *14*, 1477.
[37] S.-Y. Chung, S.-Y. Choi, T. Yamamoto, Y. Ikuhara, *Phys. Rev. Lett.* **2008**, *100*, 125502.
[38] V. Grillo, E. Rotunno, *Ultramicroscopy* **2013**, *125*, 97.
[39] J. Rodriguezcarvajal, *Physica B* **1993**, *192*, 55.
[40] P. Hohenberg, W. Kohn, *Phys. Rev.* **1964**, *136*, B864.
[41] W. Kohn, L. J. Sham, *Phys. Rev.* **1965**, *140*, A1133.
[42] B. Mennucci, *J. Phys. Chem. Lett.* **2010**, *1*, 1666.
[43] G. Kresse, J. Furthmuller, *Phys. Rev. B* **1996**, *54*, 11169.
[44] P. E. Blochl, *Phys. Rev. B* **1994**, *50*, 17953.
[45] G. Kresse, D. Joubert, *Phys. Rev. B* **1999**, *59*, 1758.
[46] J. P. Perdew, K. Burke, M. Ernzerhof, *Phys. Rev. Lett.* **1996**, *77*, 3865.
[47] A. I. Liechtenstein, V. I. Anisimov, J. Zaanen, *Phys. Rev. B* **1995**, *52*, R5467.
[48] F. Zhou, M. Cococcioni, C. A. Marianetti, D. Morgan, G. Ceder, *Phys. Rev. B* **2004**, *70*
[49] M. W. Schmidt, K. K. Baldridge, J. A. Boatz, S. T. Elbert, M. S. Gordon, J. H. Jensen, S. Koseki, N. Matsunaga, K. A. Nguyen, S. J. Su, T. L. Windus, M. Dupuis, J. A. Montgomery, *J. Comput. Chem.* **1993**, *14*, 1347.
[50] V. A. Rassolov, M. A. Ratner, J. A. Pople, P. C. Redfern, L. A. Curtiss, *J. Comput. Chem.* **2001**, *22*, 976.
[51] J. Li, C. L. Fisher, J. L. Chen, D. Bashford, L. Noodleman, *Inorg. Chem.* **1996**, *35*, 4694.
[52] P. Jaque, A. V. Marenich, C. J. Cramer, D. G. Truhlar, *J. Phys. Chem. C* **2007**, *111*, 5783.
[53] A. Klamt, G. Schuurmann, *J. Chem. Soc., Perkin Trans. 2* **1993**, 799.

Figure 1

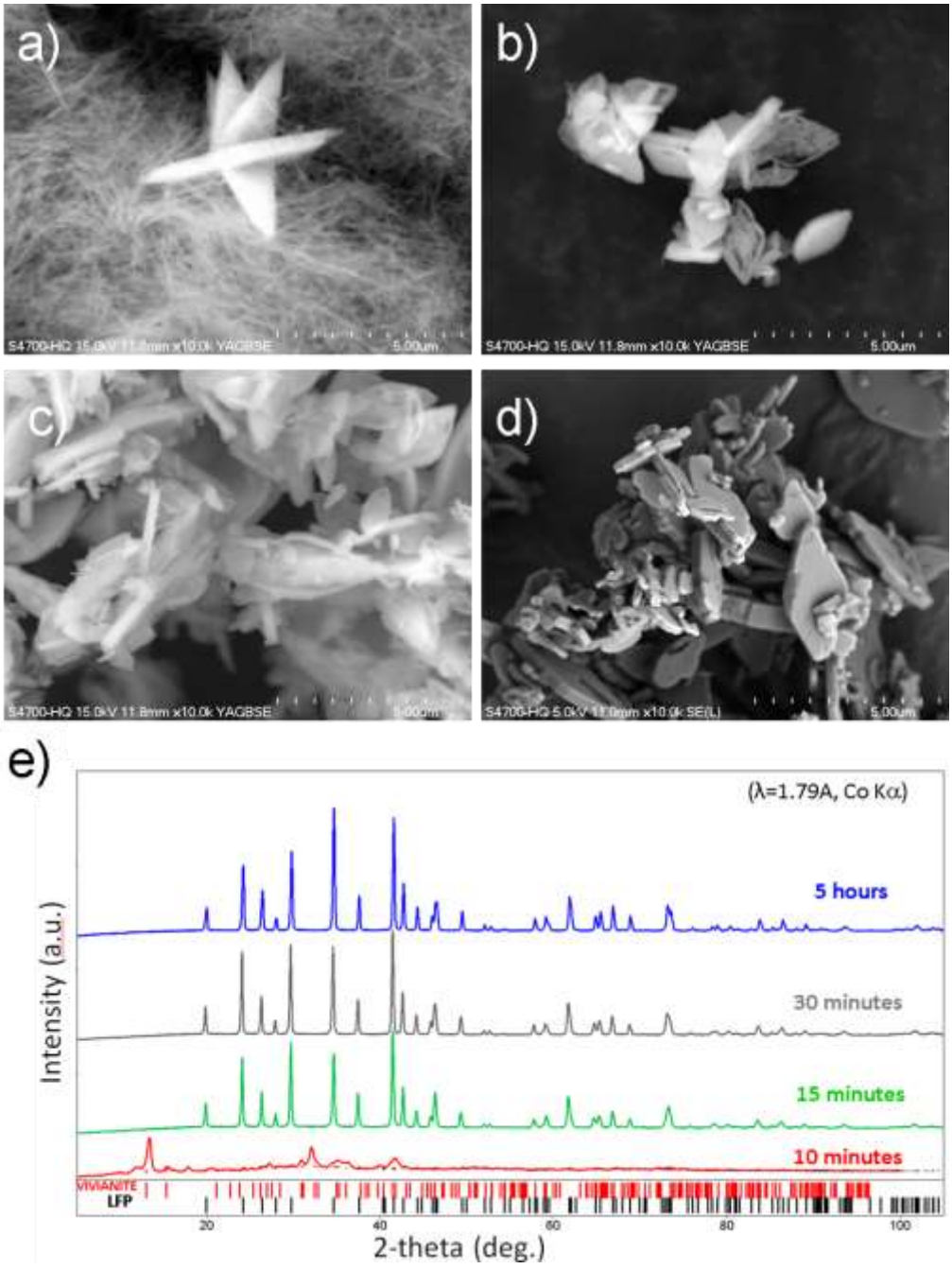
a)
b)
c)
d)
e)
(λ=1.79A, Co Kα)
5 hours
30 minutes
15 minutes
10 minutes
VIVIANITE
LFP
Intensity (a.u.)
20
40
60
80
100
2-theta (deg.)

Figure 1*: SEM image of the crystal evolution at 10 minutes a), at 15 minutes b), at 30 minutes c) and 5 hours d); e) XRD patterns for all the intermediates samples.*

Figure 2

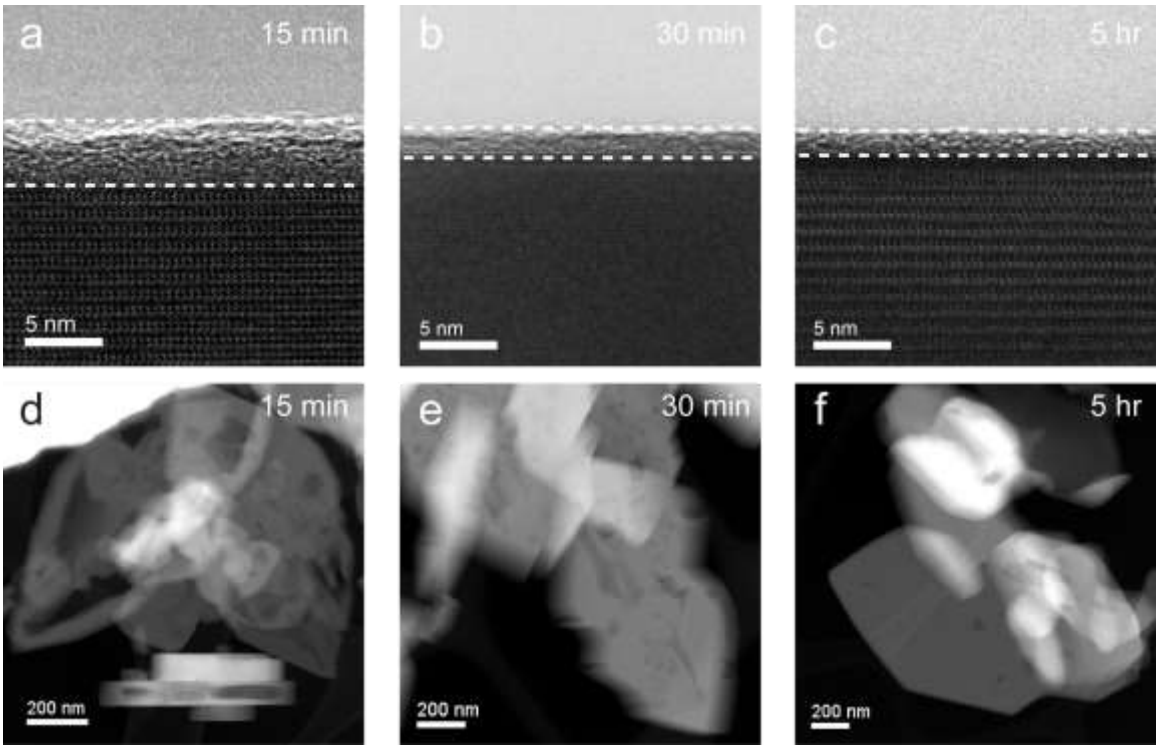

Figure 2*: Top: (a-c) HRTEM images of the surface at 15 minutes, 30 minutes, and 5 hours, Bottom: (d-f) STEM images of the evolution of $LiFePO_4$ crystals at 15 minutes, 30 minutes, and 5 hours*

Table 1

	15 min	30 min	5 hr
Fe/Li	0.93 (0.2)	0.70 (0.2)	1.08 (0.2)
Fe/P	1.33 (0.1)	1.00 (0.1)	1.04 (0.1)
Fe/O	0.25 (0.03)	0.26 (0.03)	0.27 (0.03)
a-shell (nm)	3.2 (0.9)	1.6 (0.5)	1.1 (0.2)
surface area (m^2/g)	7.3	6.3	5.4

Table 1*: (Line 1-3) Composition of the crystals as determined from EELS. The high error in the Fe/Li ratio id due to the high background signal in the spectrum at Li-K edge. (Line 4) The thickness of the amorphous is reported for comparison (see* ***Figure 2****). (Line 5) BET surface area data are reported for all the intermediate samples.*

Figure 3

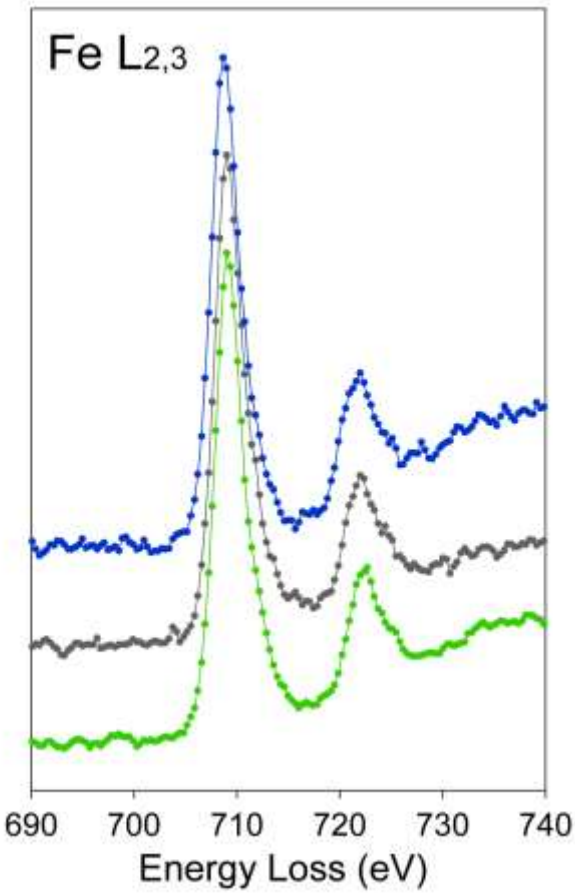

Figure 3: *EELS Fe $L_{2,3}$ ionization edges (2p→3d) as measured from the 15 minutes (green line), 30 minutes (gray line) and 5 hours (blue line) samples. The data are background subtracted in a pre-edge region and normalized to the L_3 maximum. The line shape and the L_3:L_2 ratio for the three samples are similar, and close to that of Fe+2 oxidation state.*

Figure 4

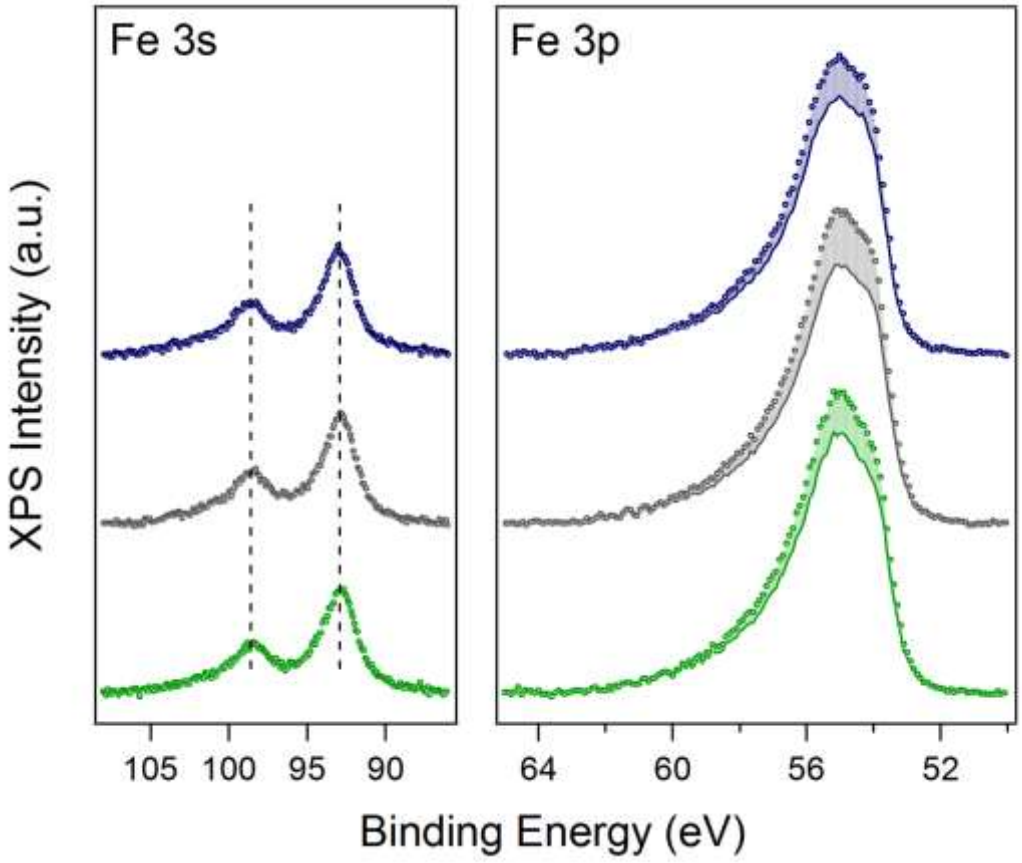

Figure 4*: XPS data collected on Fe 3s (left panel) and Fe 3p (right panel) binding energy ranges on the 15 minutes (green markers), 30 minutes (gray markers) and 5 hours (blue markers) samples. The data are reported after normalization to the area of the Fe 3s peaks and subtraction of Shirley-type background. In the right panel, together with the experimental data, scaled Fe 3p profiles (as discussed in the text) are reported. The shaded areas represent the part of the experimental profiles due to the Li content.*

Figure 5

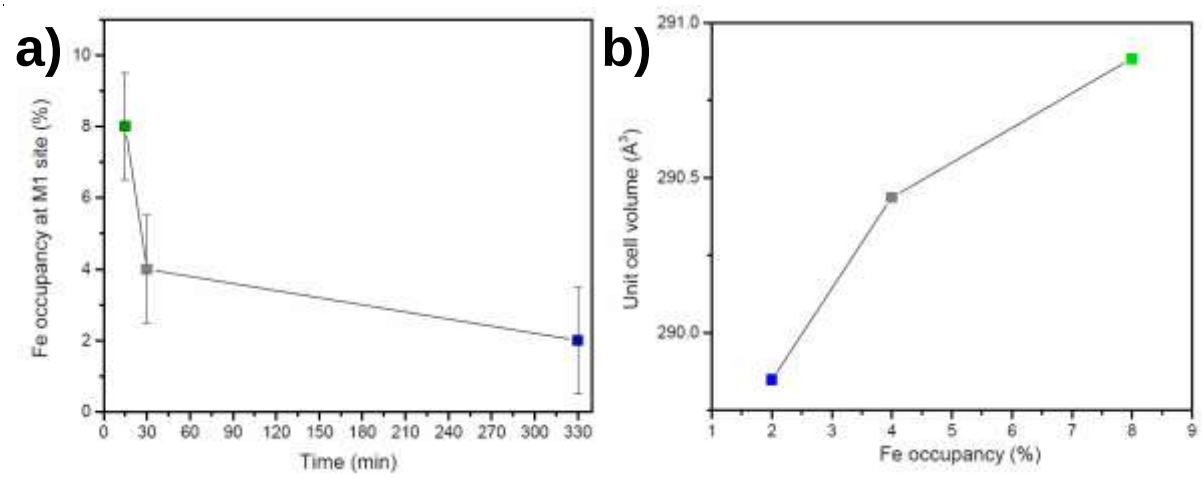

Figure 5*: a) Fe occupancy of M1 site as a function of time, b) Dependence of unit cell volume on Fe occupancy of M1 site*

Figure 6

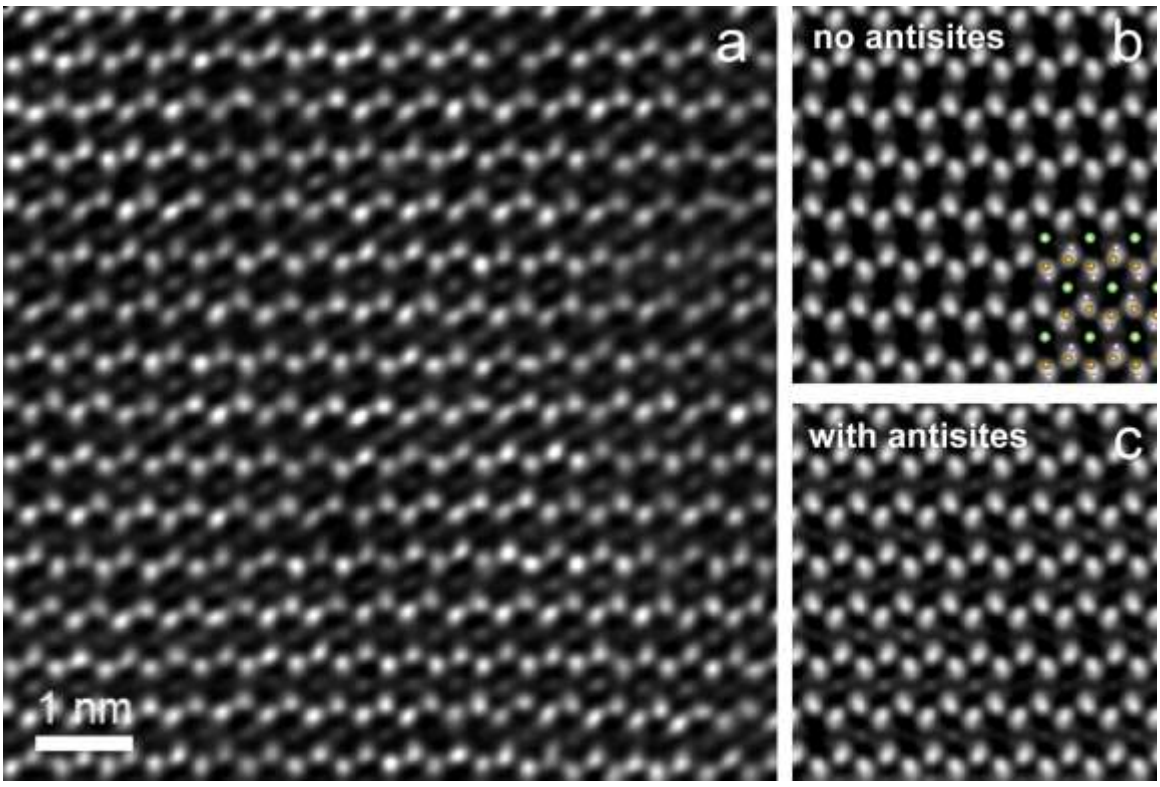

Figure 6*:* (a) *HAADF-STEM image from a 15 minutes $LiFePO_4$ crystal in [010] orientation. The bright columns are from the Fe columns at the M2 sites. Faint signals from M1 sites are visible, as resulting from the presence of Fe atoms in the columns (antisite defects). The insets (b,c) show a simulation from a perfect $LiFePO_4$ crystal with no antisite defects (b), in which the Li columns are completely dark, together with a simulation from a crystal with ~11% Fe occupancy in the M1 site (c). In the sketch Li atoms are in green, Fe in brown, and P in violet. Oxygen columns are not indicated for clarity*

Figure 7

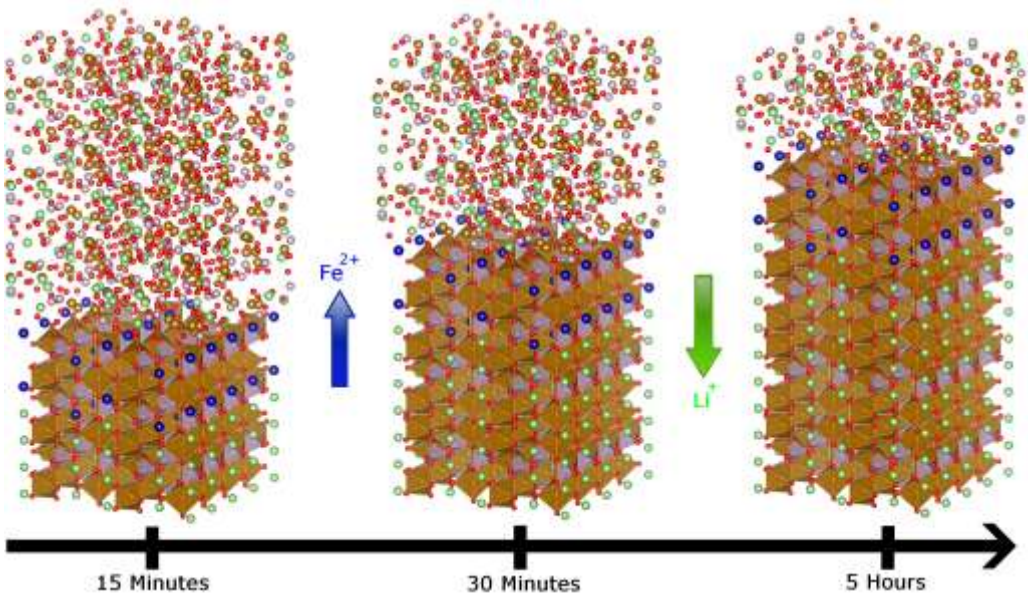

Figure 7*: schematic representation of the elimination mechanism of antisite defects in* $LiFePO_4$. *The blue spheres refer to iron ions and the green spheres are refer to lithium ion. During the synthesis there is a elimination of the antisite defects by a cation exchange involving: an intercalation of lithium ion and deintercalation of iron ions.*

Figure 8

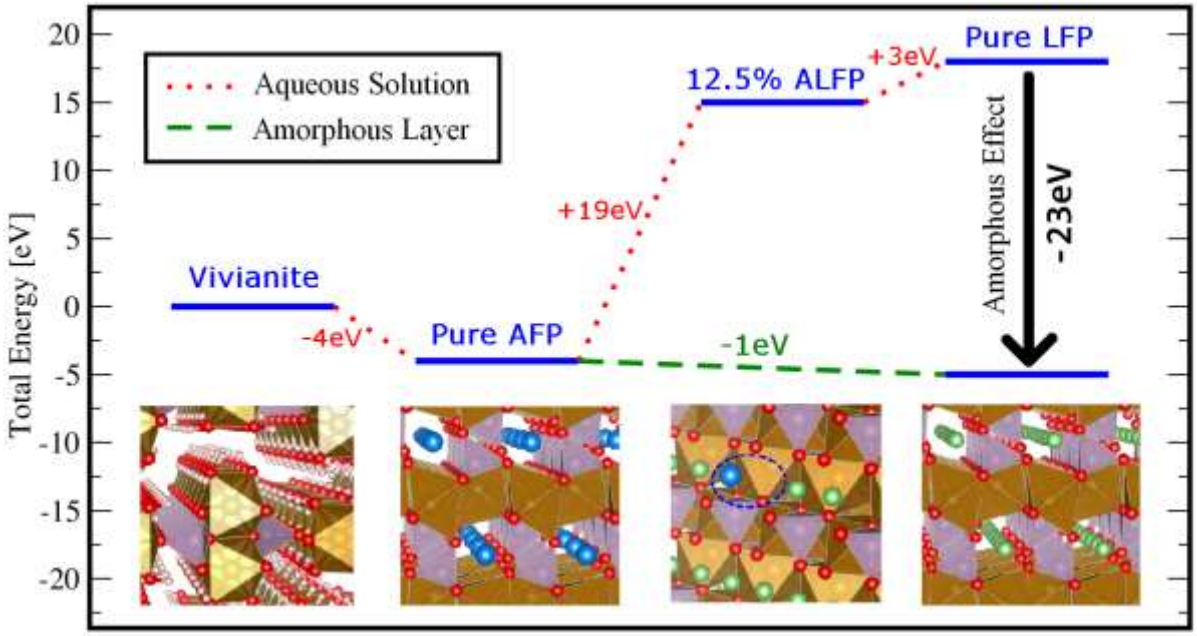

***Figure 8**: Model representing the energy level of the intermediate phase involved during the hydrothermal reaction of $LiFePO_4$. In aqueous solution (red dashed line) starting from a crystal of Vivianite $Fe_3(PO4)_2 \cdot 8H_2O$ (being the first phase formed), the orthorhombic $LiFePO_4$ fully antisite named AFP (100% of Fe in M1 lithium space) is formed easily with an energy of -4eV while a conversion to partially 12,5% Fe antisite defective $LiFePO_4$ (named ALFP) requires +19eV. A total conversion to pure $LiFePO_4$ (named LFP) requires an additional 3eV. The presence of amorphous layer (green dashed line) lowers of -23eV the total energy required for conversion to pure antisite defect free $LiFePO_4$.*

For the first time the mechanism of Fe-antisites elimination during hydrothermal synthesis of $LiFePO_4$ is described. A nanometer thick amorphous layer strict in contact with $LiFePO_4$ crystals is a reserve of lithium ions, which promotes an interfacial cation exchange reaction in order to remove the Fe-ions in antisite.

Keyword antisite, LiFePO4, hydrothermal, mechanism, amorphous

Andrea Paolella, Giovanni Bertoni, Pierre Hovington, Zimin Feng, Roxana Flacau, Mirko Prato, Massimo Colombo, Sergio Marras, Liberato Manna, Stuart Turner, Gustaaf Van Tendeloo, Abdelbast Guerfi, George P. Demopoulos and Karim Zaghib*

The Elimination Mechanism of the Fe-antisites in Hydrothermal $LiFePO_4$ synthesis